

## Quadrupole collectivity in $N \approx 28$ nuclei with the angular momentum projected generator coordinate method

R. Rodríguez-Guzmán, J. L. Egido, and L. M. Robledo

*Departamento de Física Teórica C-XI, Universidad Autónoma de Madrid, E-28049 Madrid, Spain*

(Received 20 June 2001; published 9 January 2002)

Properties of the ground and several collective excited states of selected neutron-rich  $N=28$  isotones and sulfur isotopes around  $^{44}\text{S}$  are described in the framework of the angular momentum projected generator coordinate method using the quadrupole moment as collective coordinate and the Gogny force, with the D1S parametrization, as the effective interaction. Fairly good agreement with available experimental data is obtained for the  $2^+$  excitation energies and  $B(E2)$  transition probabilities of the  $N=28$  isotones. For the sulfur isotopes an acceptable agreement is found and the isotopic trend is well reproduced. It is found that the  $N=28$  shell closure is not preserved in the prolate  $^{40}\text{Mg}$ , the oblate deformed  $^{42}\text{Si}$ , and the shape coexistent isotones  $^{44}\text{S}$  and  $^{46}\text{Ar}$ , whereas it is preserved (on the average) in  $^{48}\text{Ca}$ . The sulfur isotopes  $^{38-42}\text{S}$  are found to be, to some extent, prolate deformed.

DOI: 10.1103/PhysRevC.65.024304

PACS number(s): 21.60.Jz, 21.10.Re, 21.10.Ky, 27.30.+t

### I. INTRODUCTION

The study, both from the experimental and theoretical point of view, of the properties of neutron-rich nuclei far from stability is, nowadays, one of the most active areas of research in nuclear physics. Our knowledge of the properties of these nuclei has enormously broadened thanks to the new radioactive ion beam facilities and the development of very sophisticated isotope and fragment separators. Among the many interesting features found in the light neutron-rich nuclei, the breaking of shell closures in the  $N=20$  and  $N=28$  regions (associated with the  $f_{7/2}$  subshell) is one of the most appealing to investigate due to the insight that could be gained in the understanding of the effective interactions governing the dynamics of the nucleus. Usually, the breaking of a shell closure is associated with the appearance of deformed ground states and, in some cases, with the phenomenon of shape coexistence. The extra binding energy gained by deforming the nucleus could help to extend thereby the neutron drip line far beyond what could be expected from spherical shapes. Finally, the modifications of the nuclear decay properties brought about by deformation can substantially change our theoretical understanding of stellar nucleosynthesis processes and help us solve some of their mysteries.

It was in the neutron-rich nuclei of the  $N \approx 20$  region where the breaking of a semimagic shell closure was first found [1]. The neutron-rich nuclei with  $N \approx 20$  are spectacular examples of shape coexistence between spherical and deformed configurations and strong experimental evidence points towards the existence of a quadrupole deformed ground state in, for example,  $^{32}\text{Mg}$  [2,3]. From a shell-model point of view [4–6], the deformed ground state in  $^{32}\text{Mg}$  is a consequence of the strong correlation energy of some  $2p-2h$  neutron excitations from the  $sd$  shell into the  $pf$  shell. In the framework of the mean field theory most of the calculations carried out up to now have predicted a spherical ground state for  $^{32}\text{Mg}$ . However, when the zero point rotational energy correction is added to the mean field energy a well defined deformed minimum appears in the energy landscape [7–10].

On the other hand, the region of  $\beta$ -unstable nuclei near the  $N=28$  nucleus  $^{44}\text{S}$  has attracted particular interest because these neutron-rich nuclei play an important role in the nucleosynthesis of the heavy Ca-Ti-Cr isotopes [11]. Experimentally,  $\beta$ -decay properties of  $^{44}\text{S}$  have been studied in Refs. [11,12], and it was concluded there that the ground state of  $^{44}\text{S}$  is deformed. This conclusion has been confirmed in subsequent intermediate-energy Coulomb excitation studies [13,14] that have revealed large  $B(E2)$  values in  $^{44}\text{S}$  and in some other neutron-rich nuclei of this region. All these results suggest a significant breaking of the  $N=28$  shell closure for nuclei near  $^{44}\text{S}$ . More recent experiments [15,16] on the odd mass sulfur isotopes around  $^{44}\text{S}$  seem to indicate that  $^{44}\text{S}$  is a deformed nucleus but with strong shape coexistence whereas  $^{42}\text{S}$  can be considered as a well deformed system. These new results make the theoretical description of the neutron-rich nuclei in the  $N=28$  region even more challenging.

From a theoretical point of view, the ground state properties of nuclei around  $N=28$  have been studied by Werner *et al.* [17,18] with the Skyrme Hartree-Fock (HF) method (with the Skyrme interaction SIII [19]) as well as with the relativistic mean field (RMF) approach (with the NL-SH parameter set [20] for the mean field Lagrangian). These studies have shown the onset of deformation around  $N=28$ . A latter study based on the triaxial RMF approach without pairing and the TM1 parameter set [21] predicted the neutron-rich sulfur isotopes to be deformed. Recently, the interplay between deformed mean field and pairing correlations has been taken into account in the framework of the RMF with the NL3 effective interaction for the mean field Lagrangian and the Brink-Boeker part of the Gogny interaction (with the D1S parametrization) for the pairing channel [22]. Again, deformed shapes around  $^{44}\text{S}$  have been obtained. Another theoretical study in the framework of the Dirac-Hartree-Bogoliubov method [23] has also reached the same conclusions as the previous relativistic studies. Surprisingly, in none of these mean field calculations has the zero point rotational energy correction been considered in spite of being a

key ingredient for a proper description of the energy landscape as a function of the quadrupole deformation in this region. This is not the case, however, for the mean field calculations of Ref. [24] with several parametrizations of the Skyrme interaction and for the calculation reported in Ref. [25] in the framework of the Bohr Hamiltonian method with the Gogny interaction. In both calculations, deformation around  $^{44}\text{S}$  has also been found. The conclusion that can be extracted from all the previous results is that in the  $N=28$  region the occurrence of deformation does not depend on the rotational energy correction as crucially as in the  $N=20$  region. In this respect, it can be said that the  $N=28$  shell closure is more strongly broken than the  $N=20$  one. From the shell model point of view, the erosion of the  $N=28$  shell closure in the sulfur isotopes has also been found in calculations with the full  $sd$  shell for protons and the full  $pf$  shell for neutrons [26].

The purpose of this paper is the theoretical study of the properties of some  $N \approx 28$  nuclei focusing on their deformation properties at both  $I=0$  and  $I \neq 0$ . The considered nuclei (i.e., the sulfur isotopes  $^{38,40,42,44}\text{S}$  and the  $N=28$  isotones  $^{40}\text{Mg}$ ,  $^{42}\text{Si}$ ,  $^{44}\text{S}$ ,  $^{46}\text{Ar}$ , and  $^{48}\text{Ca}$ ) are typical examples of nuclei where the energy landscape as a function of the quadrupole moment shows either a unique but rather flat minimum or close-lying prolate and oblate minima, which are, in some cases, practically degenerate in energy. Therefore, the correlation energies associated with the restoration of broken symmetries (mainly the rotational symmetry) and/or the collective quadrupole motion have to be considered. In the present paper both effects are accounted for in the framework of the angular momentum projected generator coordinate method using the Gogny interaction [27] with the parametrization D1S [28]. The reason to carry out an exact angular momentum projection is that the usual approximations used to estimate the rotational energy correction stemming from the restoration of the rotational energy as well as the  $B(E2)$  transition probabilities are not expected, *a priori*, to work well for soft light nuclei like the ones considered here.

The use of the Gogny force in this study is supported not only by the fact that this interaction has been able to provide reasonable results for many nuclear properties all over the periodic table, but also by the good description of the phenomenology of quadrupole collectivity in the region  $N \approx 20$  obtained recently in the same framework as the one used in the present study [29–31] as well as in the context of the Bohr collective Hamiltonian [25,32]. Besides, recent results for the predicted superdeformed band in  $^{32}\text{S}$  [33] also point towards the versatility of this effective interaction in regions of the nuclear chart not yet sufficiently explored. As the results presented in this paper will show, this force is also well suited for the description of quadrupole collectivity in  $N \approx 28$  nuclei.

The paper is organized as follows. In Sec. II, we briefly summarize the theoretical formalism used in the paper. This formalism is the angular momentum projected generator coordinate method with the axial quadrupole moment as the generating coordinate and restricted to  $K=0$  configurations. In Sec. III, we discuss the results of our calculations. These

calculations have been done in different steps, which are presented in different sections. In Sec. III A, we present the results of the underlying mean field studies. In Sec. III B, we present the results coming from the angular momentum projection after variation study of the potential energy surfaces in these nuclei, and there we discuss the topological changes introduced in the mean field potential energy surfaces due to the exact restoration of the rotational symmetry. In Sec. III C, we show the results of the angular momentum projected configuration mixing calculations. In Sec. IV we compare the results for the  $2^+$  excitation energies and  $B(E2)$  transition probabilities with the available experimental data and other theoretical calculations. Finally, Sec. V is devoted to the conclusions.

## II. THEORETICAL FRAMEWORK

To study the properties of the ground and several collective excited states of the nuclei considered in this paper we have used the angular momentum projected generator coordinate method (AMPGCM) with the mass quadrupole moment as generating coordinate. The same technique has proven to successfully describe the phenomenology of other neutron-rich light nuclei [30,31,33–35]. In the AMPGCM, the following ansatz for the  $K=0$  wave functions of the system is used:

$$|\Psi^I_\sigma\rangle = \int dq_{20} f^I_\sigma(q_{20}) \hat{P}^I_{00} |\varphi(q_{20})\rangle. \quad (2.1)$$

Here  $|\varphi(q_{20})\rangle$  is the set of axially symmetric (i.e.,  $K=0$ ) Hartree-Fock-Bogoliubov (HFB) wave functions generated by HFB mean field calculations with the corresponding constraint on the mass quadrupole moment  $q_{20} = \langle \varphi(q_{20}) | z^2 - \frac{1}{2}(x^2 + y^2) | \varphi(q_{20}) \rangle$  [45]. Extending the set of intrinsic states to include triaxial configurations would be desirable but it would imply a full triaxial projection, which is computationally far too much time consuming compared to the present approach. An additional restriction is that reflection symmetry has also been imposed as a self-consistent symmetry of the generating states  $|\varphi(q_{20})\rangle$ . Therefore, we are limited to the study of positive parity and even spin states. As it is customary, the integral of Eq. (2.1) has been discretized with a step size  $\Delta q_{20}$  of 10 fm<sup>2</sup>, which yields to typical overlaps  $\langle \varphi(q_{20}) | \varphi(q_{20} + \Delta q_{20}) \rangle$  of around 0.95.

The intrinsic wave functions  $|\varphi(q_{20})\rangle$  have been expanded in a ten-major-shell harmonic oscillator (HO) basis with equal oscillator lengths. The use of equal oscillator lengths is not the optimal one but it is mandatory in order to maintain the basis closed under rotations [36,37]. Adding one more shell to the basis increases enormously the computational time needed to evaluate the projected Hamiltonian kernels (typically a factor of 10, from three days to one month in a typical workstation). However, it is important (especially for very neutron-rich nuclei) to check the stability of the results with the size of the basis. To this end, we have repeated the calculations for one of the nuclei ( $^{40}\text{Mg}$ ) with eleven shells and found no significant differences (see below) with the  $N_{\text{osc}}=10$  case.

The rotation operator in the HO basis has been computed using the formulas of Ref. [38]. The operator  $\hat{P}_{00}^I$  is the usual angular momentum projector [39,40] with the  $K=0$  restriction and  $f_\sigma^I(q_{20})$  are the collective amplitudes which are solutions of the Hill-Wheeler (HW) equation

$$\int dq'_{20} [\mathcal{H}^I(q_{20}, q'_{20}) - E_\sigma^I \mathcal{N}^I(q_{20}, q'_{20})] f_\sigma^I(q'_{20}) = 0. \quad (2.2)$$

The quantities

$$\mathcal{H}^I(q_{20}, q'_{20}) = \langle \varphi(q_{20}) | \hat{H} \hat{P}_{00}^I | \varphi(q'_{20}) \rangle \quad (2.3)$$

and

$$\mathcal{N}^I(q_{20}, q'_{20}) = \langle \varphi(q_{20}) | \hat{P}_{00}^I | \varphi(q'_{20}) \rangle \quad (2.4)$$

are the Hamiltonian and norm kernels, respectively. In order to account for the fact that the expectation value of the particle number operator usually differs from the nucleus' proton and neutron numbers, we have followed the usual recipe of Refs. [29,30,33,41,42] and replaced the Hamiltonian by  $\hat{H} - \lambda_Z(\hat{Z} - Z_0) - \lambda_N(\hat{N} - N_0)$ , where  $\lambda_Z$  and  $\lambda_N$  are chemical potentials for protons and neutrons, respectively.

As it is well known, the GCM amplitudes  $f^{I,\sigma}(q_{20})$  cannot be interpreted as probability amplitudes due to the lack of orthogonality of the generating states  $|\varphi(q_{20})\rangle$ , that is,  $\mathcal{N}(q_{20}, q'_{20}) \equiv \langle \varphi(q_{20}) | \varphi(q'_{20}) \rangle \neq \delta(q_{20} - q'_{20})$ . In order to define a probability amplitude, one has first to orthogonalize the generating states in order to get the set of orthogonal states

$$|\vartheta(q_{20})\rangle = \int dq'_{20} \mathcal{N}^{*-1/2}(q_{20}, q'_{20}) |\varphi(q'_{20})\rangle$$

and then express  $|\Psi_\sigma^I\rangle$  as a linear combination of them,

$$|\Psi_\sigma^I\rangle = \int dq_{20} g_\sigma^I(q_{20}) |\vartheta(q_{20})\rangle$$

with

$$g_\sigma^I(q_{20}) = \int dq'_{20} f_\sigma^I(q'_{20}) \mathcal{N}^{*1/2}(q_{20}, q'_{20}). \quad (2.5)$$

The set of functions  $g_\sigma^I(q_{20})$  is orthonormal,

$$\int dq_{20} g_\sigma^{I*}(q_{20}) g_{\sigma'}^I(q_{20}) = \delta_{\sigma,\sigma'},$$

and therefore its modulus squared can be interpreted as a probability amplitude.

For the density-dependent part of the Gogny force we have used the prescription already discussed in Refs. [29,30,33–35,42]. This prescription amounts to using the density

$$\bar{\rho}_\beta(\vec{r}) = \frac{\langle \varphi(q_{20}) | \hat{\rho} e^{-i\beta \hat{J}_y} | \varphi(q'_{20}) \rangle}{\langle \varphi(q_{20}) | e^{-i\beta \hat{J}_y} | \varphi(q'_{20}) \rangle} \quad (2.6)$$

in the density-dependent part of the interaction when the evaluation of the Hamiltonian kernel is required.

The HW equation provides, for each angular momentum  $I$ , the ground state ( $\sigma=1$ ) and also excited states ( $\sigma=2,3,\dots$ ) that, with the set of generating functions considered,  $|\varphi(q_{20})\rangle$ , could correspond to states with a deformation different from the one of the ground state (shape isomers) and/or to quadrupole vibrational states.

One of the main motivations for carrying out exact angular momentum projected configuration-mixing calculations is that they allow the exact evaluation of the electromagnetic transition probabilities. In addition, the Gogny force is defined in the full configuration space, that is, not only the valence particles but also the core ones have to be fully taken into account. Therefore the introduction of effective charges is not required in our formalism. A detailed derivation of the corresponding expressions will be presented in a subsequent publication and here only the final result for the axially symmetric case and the  $B(E2)$  transition probability is given:

$$B(E2, I_i \sigma_i \rightarrow I_f \sigma_f) = \frac{e^2}{2I_i + 1} \left| \int dq_{20} dq'_{20} f_{\sigma_f}^{I_f*}(q'_{20}) \times \langle I_f q'_{20} | \hat{Q}_2 | I_i q_{20} \rangle f_{\sigma_i}^{I_i}(q_{20}) \right|^2. \quad (2.7)$$

In the above expression, the indices  $i$  and  $f$  stand for the initial and final states and  $\hat{Q}_{2\mu}$  are the charge quadrupole moment operators. The reduced matrix elements  $\langle I_f q'_{20} | \hat{Q}_2 | I_i q_{20} \rangle$  are given by

$$\begin{aligned} & \langle I_f q'_{20} | \hat{Q}_2 | I_i q_{20} \rangle \\ &= \frac{(2I_i + 1)(2I_f + 1)}{2} (-1)^{I_i - 2} \sum_{\mu'} \begin{pmatrix} I_i & 2 & I_f \\ -\mu' & \mu' & 0 \end{pmatrix} \\ & \times \int_0^\pi d\beta \sin \beta d_{-\mu' 0}^{I_i}(\beta) \\ & \times \langle \varphi(q'_{20}) | \hat{Q}_{2\mu'} e^{-i\beta \hat{J}_y} | \varphi(q_{20}) \rangle. \end{aligned} \quad (2.8)$$

In the same way we can compute the spectroscopic quadrupole moment  $Q^{\text{spect}}(I, \sigma)$  (for each of the states  $|\Psi_\sigma^I\rangle$  and  $I \geq 2$ ), which is given by

$$\begin{aligned} Q^{\text{spect}}(I, \sigma) &= e \sqrt{\frac{16\pi}{5}} \begin{pmatrix} I & 2 & I \\ I & 0 & -I \end{pmatrix} \int dq_{20} dq'_{20} f_\sigma^{I*}(q'_{20}) \\ & \times \langle I q_{20} | \hat{Q}_2 | I q'_{20} \rangle f_\sigma^I(q'_{20}). \end{aligned} \quad (2.9)$$

### III. DISCUSSION OF THE RESULTS

In this section we describe our results for the set of nuclei considered. The mean field approximation is our starting point and will be described first while the many-body effects beyond the mean field (i.e, angular momentum projection and configuration mixing) will be described in the later sections.

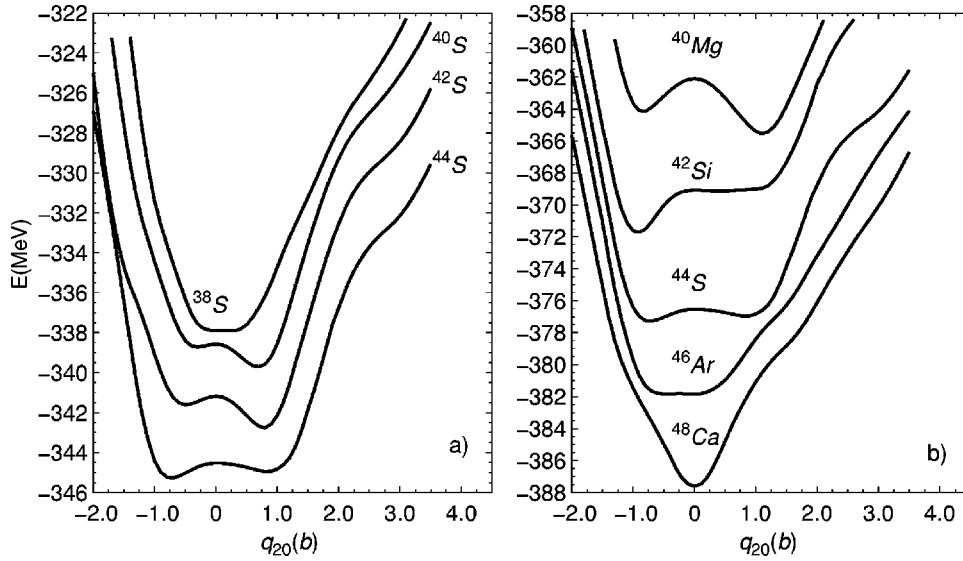


FIG. 1. Mean field potential energy surfaces for the nuclei  $^{38,40,42,44}\text{S}$  [panel (a)] and  $^{40}\text{Mg}$ ,  $^{42}\text{Si}$ ,  $^{44}\text{S}$ ,  $^{46}\text{Ar}$ , and  $^{48}\text{Ca}$  [panel (b)]. All the curves have been shifted by the corresponding amount for each nucleus to fit them in a single plot. In panel (a) the energy shifts are  $-3$ ,  $-8$ ,  $-15$ , and  $-25$  MeV for  $^{44,42,40,38}\text{S}$ , whereas in panel (b) the energy shifts are  $+20$ ,  $-5$ ,  $-35$ ,  $-68$ , and  $-110$  MeV for  $^{48}\text{Ca}$ ,  $^{46}\text{Ar}$ ,  $^{44}\text{S}$ ,  $^{42}\text{Si}$ , and  $^{40}\text{Mg}$ , respectively.

### A. Mean field description

The most relevant quantities obtained in the mean field calculations are shown in Figs. 1 and 2. In Fig. 1 the mean field potential energy surfaces (MFPEs) are shown for  $^{38,40,42,44}\text{S}$  in panel (a) and for  $^{40}\text{Mg}$ ,  $^{42}\text{Si}$ ,  $^{44}\text{S}$ ,  $^{46}\text{Ar}$ ,  $^{48}\text{Ca}$  in panel (b). The MFPEs do not include the Coulomb exchange energy.

We observe in panel (a) of Fig. 1 that the nucleus  $^{38}\text{S}$  is a deformation soft system. Its ground state is prolate ( $\beta_2 = 0.07$ ) but is only 23 keV deeper than the spherical maximum. The nuclei  $^{40,42}\text{S}$  are also prolate deformed with  $\beta_2 = 0.24$  and  $0.25$ , respectively. Both nuclei also show oblate local minima located at  $\beta_2 = -0.10$  for  $^{40}\text{S}$  and  $\beta_2 = -0.16$  for  $^{42}\text{S}$  and with excitation energies, with respect to the prolate ground states, of 979 keV and 1.17 MeV, respectively. On the other hand,  $^{44}\text{S}$  is found to be oblate ( $\beta_2 = -0.20$ ) with a prolate local minimum at  $\beta_2 = 0.23$  with an excitation energy of 310 keV.

In panel (b) of Fig. 1 we observe that the nucleus  $^{40}\text{Mg}$  has a prolate ground state ( $\beta_2 = 0.33$ ) and an oblate local minimum ( $\beta_2 = -0.25$ ), which is 1.38 MeV higher. The nucleus  $^{42}\text{Si}$  shows a well-defined oblate ground state ( $\beta_2 = -0.27$ ) that is 2.65 MeV deeper than the spherical configuration. Finally, both  $^{46}\text{Ar}$  and  $^{48}\text{Ca}$  are spherical systems and the nucleus  $^{46}\text{Ar}$  shows a deformation soft behavior.

To check the stability of our calculations with the basis size we have carried out calculations with eleven shells for the nucleus  $^{40}\text{Mg}$ . The energy gain obtained by increasing the basis size depends on the quadrupole deformation and ranges from 98 keV for the prolate minimum to almost 1 MeV for the highest deformation attained. However, the energy gain in the relevant interval around the minima ( $q_{20}$  between  $-1.25$  b and  $1.75$  b) never exceeds 200 keV. In the next section we will discuss the effect of increasing the basis in the GCM calculations.

The particle-particle correlation energies  $E_{pp} = -\frac{1}{2} \text{Tr}(\Delta \kappa^*)$  for both protons and neutrons are presented in Fig. 2. As can be observed in the figure, the evolution of the particle-particle correlation energies is well correlated with

the structures found in the MFPEs. Pairing correlations are significantly reduced in the vicinity of the minima due to the reduction of the single-particle level density and in some cases both proton and neutron pairing correlations become zero at the minima of the MFPEs. The unphysical collapse of pairing correlations clearly indicates that dynamical pairing correlations could play an important role in the collective dynamics of these nuclei. At present, dynamical pairing is not included in our treatment of the problem and this is probably the most important drawback of our calculations. Work is in progress in order to incorporate the dynamical interplay between the quadrupole and the pairing degrees of freedom.

Another interesting piece of information coming from the mean field are the single-particle energies for protons and neutrons. In our calculations we are solving the HFB equation and therefore the only quantities that can be properly defined are the quasiparticle energies. However, in order to have the more usual, Nilsson-like, single-particle energy diagram (which shows, for instance, which levels are occupied and which ones are empty), we have chosen to plot the eigenvalues of the Hartree-Fock Hamiltonian  $h = T + \Gamma$  as a function of the quadrupole deformation. As an illustrative example, we show in Fig. 3 the single-particle diagrams for protons and neutrons for the nucleus  $^{42}\text{S}$ .

From the SPE diagram we can understand in a qualitative way (one has to keep in mind that the HF energy is given by the sum of the single-particle energies minus the interaction energy  $\frac{1}{2} \Gamma_{ii}$ ) the behavior of the MFPEs of the nuclei considered. For instance, in going from  $^{40}\text{Mg}$  to  $^{42}\text{Si}$  we occupy the proton  $\Omega = 5/2$  orbital from the  $d_{5/2}$  subshell, and, as this orbital increases its energy as the quadrupole moment increases, the prolate minimum in  $^{40}\text{Mg}$  is no longer present in  $^{42}\text{Si}$ . Only the oblate minimum remains in the latter nucleus. Adding another two protons (to create  $^{44}\text{S}$ ) we occupy the  $2s_{1/2}$  orbital, which increases its energy, in the oblate side, as the quadrupole deformation decreases. Therefore, the oblate minimum present in  $^{42}\text{Si}$  is washed out in  $^{44}\text{S}$ . The addition of another two protons ( $^{46}\text{Ar}$ ) populates the  $d_{3/2}$  orbital, which increases its energy as the absolute value of the quad-

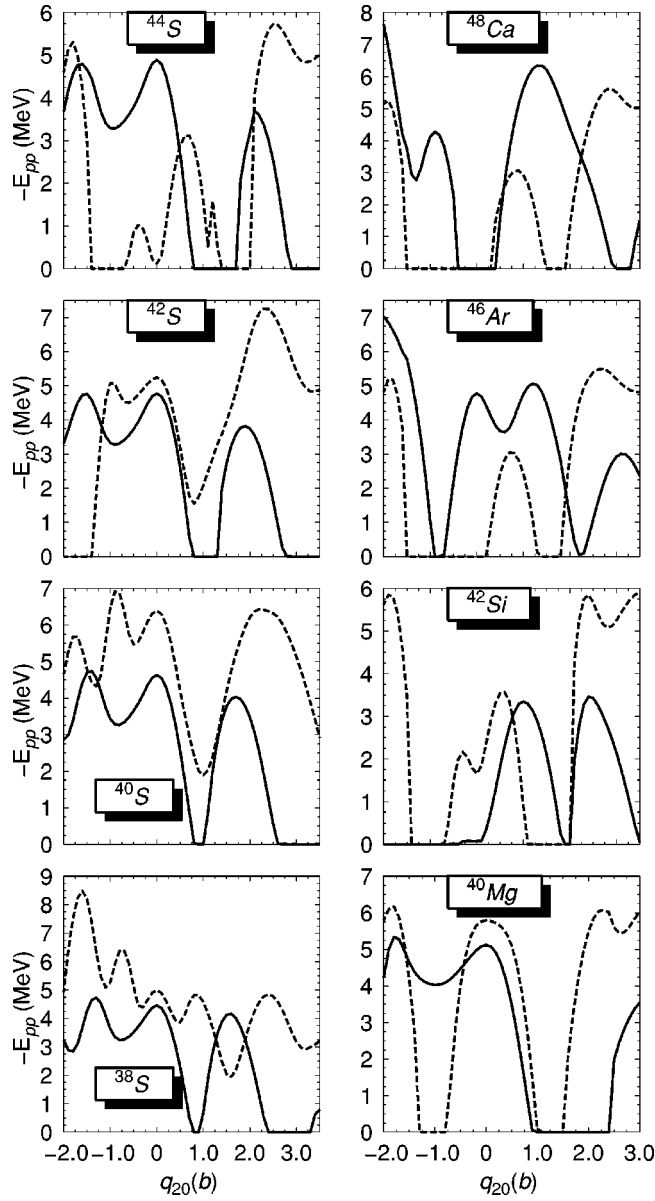


FIG. 2. Mean field particle-particle correlation energies for protons (solid line) and neutrons (dashed line) for the nuclei  $^{38,40,42,44}\text{S}$  (panels on the left) and  $^{40}\text{Mg}$ ,  $^{42}\text{Si}$ ,  $^{46}\text{Ar}$ ,  $^{48}\text{Ca}$  (panels on the right).

rupole deformation increases, and therefore the MFPES only has a spherical minimum. The addition of another two protons ( $^{48}\text{Ca}$ ) completely populates the  $d_{3/2}$  subshell and therefore the situation is similar to the one in  $^{46}\text{Ar}$ .

On the neutron side, adding two neutrons to  $^{42}\text{S}$  implies occupying the  $\Omega = 7/2$  orbital from the  $f_{7/2}$  subshell. As the energy of this orbital increases as the quadrupole moment increases, the prolate minimum in  $^{42}\text{S}$  disappears in  $^{44}\text{S}$ . For the nuclei  $^{38}\text{S}$  and  $^{40}\text{S}$  the situation is not so clear and here the role of the interaction energy determines the appearance of the minima.

In the literature there are many mean field calculations on the nuclei considered in this paper that have explored a variety of interactions in the particle-hole channel (both relativistic and nonrelativistic) as well as a variety of choices for

the particle-particle channel. It is not the purpose of this paper to compare the different results obtained up to date but we would like to mention some characteristic features found in all the mean field calculations: In most of the calculations the nuclei  $^{40}\text{Mg}$ ,  $^{40}\text{S}$ , and  $^{42}\text{S}$  are clearly prolate deformed, the nucleus  $^{42}\text{Si}$  is clearly oblate deformed, the nuclei  $^{38}\text{S}$  and  $^{44}\text{S}$  show shape coexistence, and finally the nuclei  $^{46}\text{Ar}$  and  $^{48}\text{Ca}$  are spherical.

At this point it has to be said that, as the results of the next sections will show, the mean field is just a starting point and additional correlations have to be incorporated in order to properly describe the nuclei considered. The small energy differences observed between the coexisting minima in the MFPES and also the fact that the MFPES are very flat around the corresponding minima clearly indicate that many-body effects beyond the mean field, such as restoration of the broken rotational symmetry and/or quadrupole fluctuations, may change the conclusions extracted from the raw HFB approximation. The restoration of the rotational energy leads to an energy gain (the so called rotational energy correction), which is proportional to the quadrupole deformation of the intrinsic state and ranges from zero (spherical intrinsic state) to a few MeV for typical well-deformed configurations in this region of the periodic table. Therefore, taking it into consideration can substantially modify the mean field energy landscape as is discussed in the next section. In addition to the rotational energy correction, it is important to consider the effect of quadrupole mixing in those cases where coexisting quadrupole minima appear. The configuration mixing can again substantially modify the deformation of the ground and excited states.

### B. Angular momentum projected description

In this section we consider the effect of the restoration of the rotational symmetry on the energy landscapes of the nuclei considered. In Figs. 4 and 5 we present the angular momentum projected potential energy surfaces (AMPES),

$$E^I(q_{20}) = \frac{\mathcal{H}^I(q_{20}, q_{20})}{\mathcal{N}^I(q_{20}, q_{20})},$$

as a function of  $q_{20}$ , for spins  $I = 0, 2, 4, 6$ , and  $8$  and all the nuclei studied. Before discussing the physical contents of the AMPES of Figs. 4 and 5, we have to mention that for  $I \neq 0$  several values around the spherical configuration (which is already a pure  $0^+$  state) have been omitted. They correspond to intrinsic configurations with very small values of the projected norm  $\mathcal{N}^I(q_{20}, q_{20})$  for which the evaluation of the projected energies is vulnerable to strong numerical inaccuracies. Fortunately, these configurations do not play a role in the configuration mixing calculation and therefore can be safely omitted [29,30,33,35].

In both figures we observe that for  $I = 0$  the AMPES considerably differ from the MFPES, reflecting the importance of considering the effect of the restoration of the rotational symmetry on the energy. In all the cases we observe a prolate and an oblate minimum separated by a barrier with its maximum at  $q_{20} = 0$ . In the four sulfur isotopes studied

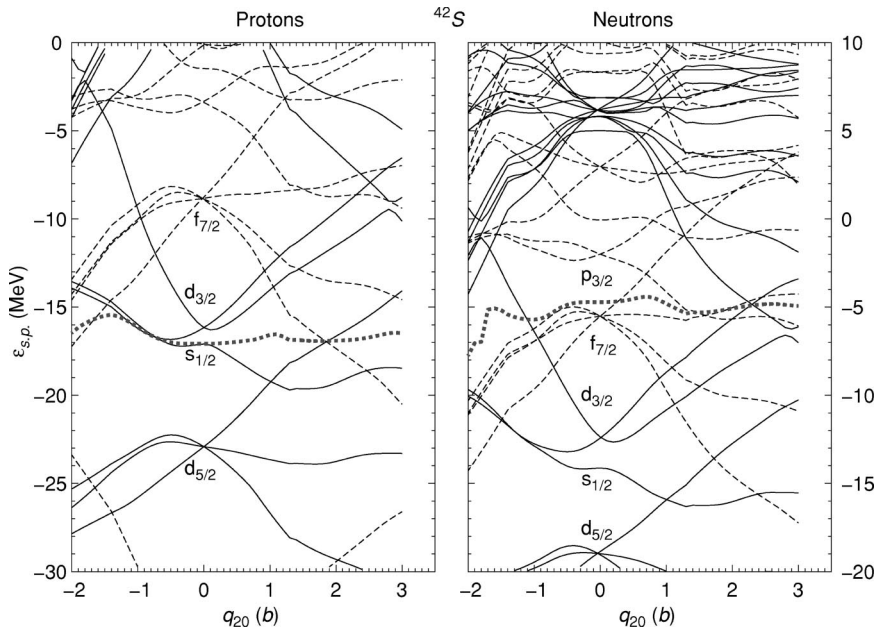


FIG. 3. Proton and neutron single particle diagrams as a function of the quadrupole deformation for the nucleus  $^{42}\text{S}$ . Full (dashed) lines correspond to positive (negative) parity levels. The Fermi levels are represented as thick dotted lines. Also shown are the spherical quantum numbers at  $q_{20}=0$ .

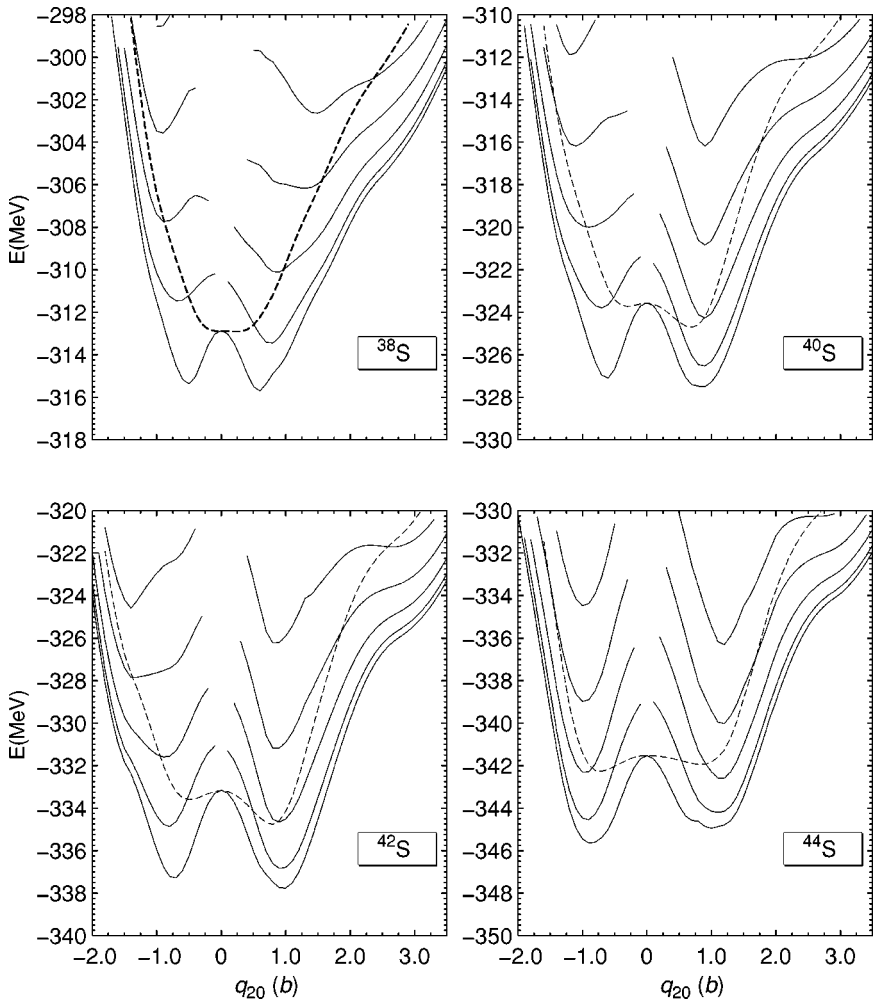


FIG. 4. Angular momentum projected potential energy surfaces for the nuclei  $^{38,40,42,44}\text{S}$  (full lines) along with the mean field results (dashed curves). In all the nuclei the angular momentum of the curves correspond, from bottom to top, to  $I=0, 2, 4, 6,$  and  $8$ .

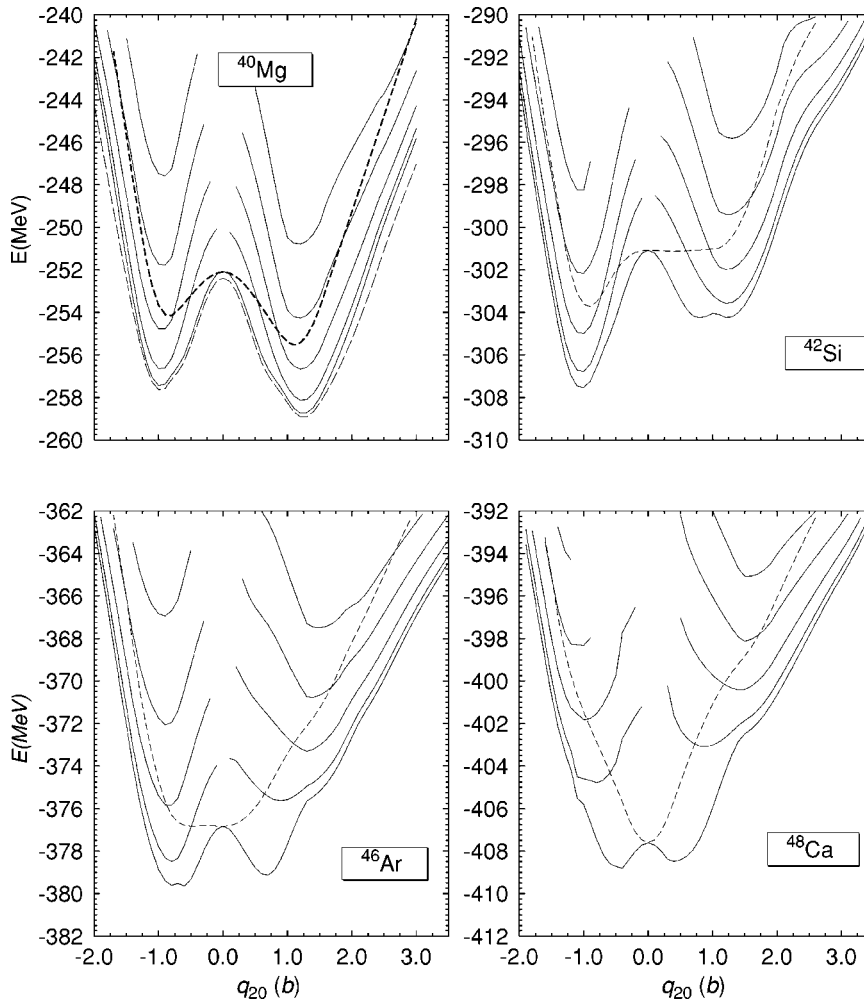


FIG. 5. Same as Fig. 4 but for the nuclei  $^{40}\text{Mg}$ ,  $^{42}\text{Si}$ ,  $^{46}\text{Ar}$ , and  $^{48}\text{Ca}$ .

the prolate and oblate minima lie very close in energy for  $I = 0$  but are separated by a rather high barrier. Therefore, it is difficult to assert beforehand whether the effect of configuration mixing (i.e., tunneling through the barrier) is important or not. In the next section we will discuss such effects and we will come to the conclusion that configuration mixing is very important indeed for the description of the  $I = 0$  ground state of the sulfur isotopes considered. On the other hand, we observe that for spin values  $I \geq 2$  the prolate minima, as compared to the oblate ones, become deeper than for  $I = 0$  in  $^{38,40,42}\text{S}$ . For example, the energy difference between the prolate and the oblate minima in  $^{38}\text{S}$  at spin  $I = 2$  is around 2 MeV while for spin  $I = 8$  this difference is around 4 MeV. However, in  $^{44}\text{S}$  both the  $I = 0$  and the  $I = 2$  AMPPES show an absolute minimum corresponding to oblate deformations, but one should note that at spin  $I = 4$  a band crossing takes place and the prolate band becomes yrast. The present calculations suggest that all the sulfur isotopes studied are dominated by prolate deformations as the spin is increased.

The corresponding results for the  $N = 28$  isotones are presented in Fig. 5. From this plot we conclude that at  $I = 0$  and owing to the barrier heights separating the prolate and oblate minima, the ground state of  $^{40}\text{Mg}$  will be prolate deformed and that of  $^{42}\text{Si}$  will be oblate deformed. Nothing can be said

concerning  $^{44}\text{S}$ ,  $^{46}\text{Ar}$ , and  $^{48}\text{Ca}$  as shape coexistence could be a very important ingredient. In the panel corresponding to  $^{40}\text{Mg}$  we have also included the  $I = 0$  results obtained with eleven shells (dashed line). We observe no noticeable difference between the results with ten and eleven shells in the relevant regions around the minima.

As a general rule we observe that as the spin increases the prolate and oblate wells are deeper and the barriers separating them become higher, making the corresponding minima more stable against axially symmetric quadrupole fluctuations. The ground state band in  $^{46}\text{Ar}$  and  $^{48}\text{Ca}$  is oblate up to spin  $I = 6$  and then it is crossed by the prolate band, which becomes yrast. Both  $^{40}\text{Mg}$  and  $^{42}\text{Si}$  are dominated by deformations of the same type (prolate in  $^{40}\text{Mg}$  and oblate in  $^{42}\text{Si}$ ) all over the considered spin range.

### C. Angular momentum projected configuration mixing

As it was previously discussed, the AMPPES for some angular momentum values and nuclei show the phenomenon of shape coexistence, and therefore configuration mixing is needed to disentangle the structure of the states. Even in those situations where the potential energy curves show a relatively well-pronounced minimum, it is always interesting to check the results of the configuration mixing calculations.

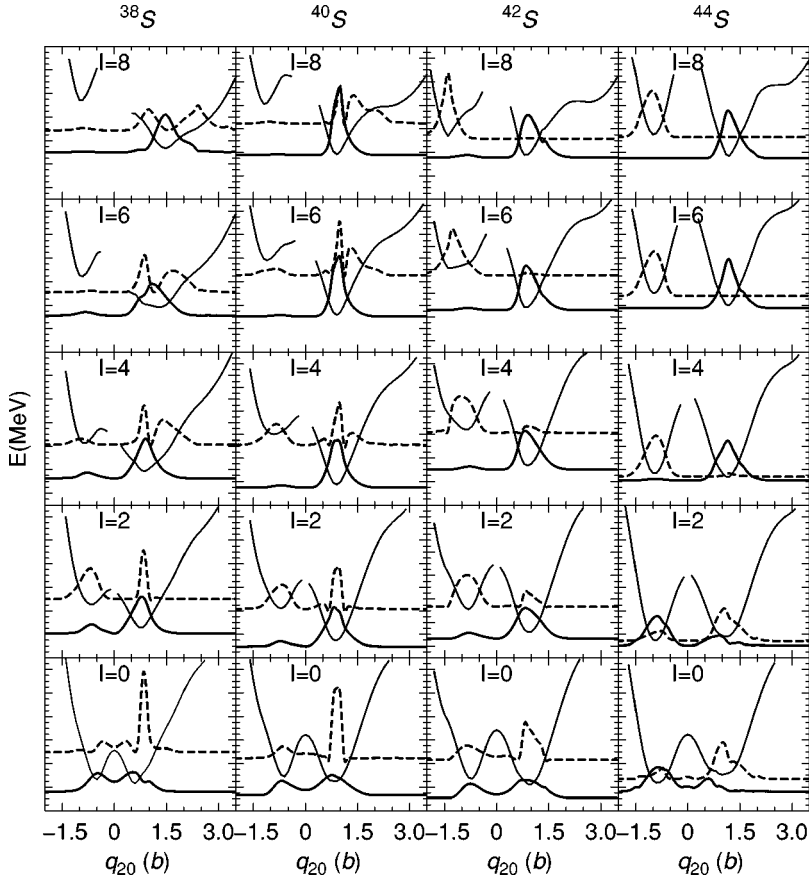


FIG. 6. The collective amplitudes  $|g_{\sigma}^I(q_{20})|^2$  (thick lines) for  $\sigma=1$  and  $\sigma=2$  and spin values  $I=0\hbar, \dots, 8\hbar$  for the nuclei  $^{38,40,42,44}\text{S}$ . The AMPPES for each spin are also plotted. The y-axis scales are in energy units and always span an energy interval of 13 MeV (minor ticks are 0.5-MeV apart). The collective wave functions  $|g_{\sigma}^I(q_{20})|^2$  have also been plotted against the energy after a proper scaling and shifting, that is, the quantity  $E_{\sigma}^I + 15|g_{\sigma}^I(q_{20})|^2$  is the one actually plotted. With this choice for scales we can read from the figure the energy gain due to the quadrupole fluctuations by considering the position of the wave functions' tail relative to the AMPPES.

The reason is that not only the potential energy plays a role in the description of the dynamics of the system but also the collective inertia has to be considered. If the collective inertia shows sudden changes as a function of  $q_{20}$  it might influence more strongly the collective dynamics than the potential energy surface. Therefore, we have performed angular momentum projected generator coordinate method (AMPGCM) calculations along the lines described in Sec. II using as the generating coordinate the intrinsic quadrupole moment  $q_{20}$ . After solving the Hill-Wheeler equation [Eq. (2.2)] for each angular momentum  $I$  we obtain a set of states with energies  $E_{\sigma}^I$  and collective amplitudes  $|g_{\sigma}^I(q_{20})|^2$ . In Figs. 6 and 7 we show the collective wave functions squared  $|g_{\sigma}^I(q_{20})|^2$  [see Eq. (2.5)] obtained in the AMPGCM calculations for the two lowest solutions  $\sigma=1$  and  $\sigma=2$ , the range of spins  $I=0, \dots, 8$ , and all the nuclei considered in the previous section. To guide the eye we also show in each panel the AMPPES for the corresponding spin.

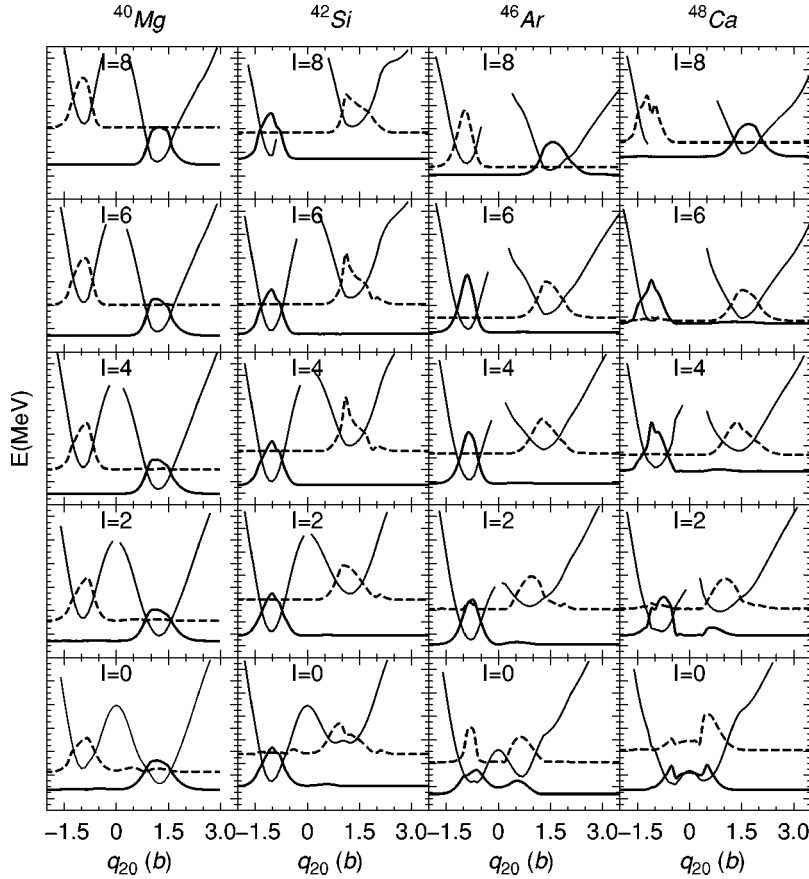
We observe that the  $0_1^+$  ground states in  $^{38,40,42,44}\text{S}$  and also in  $^{46}\text{Ar}$  and  $^{48}\text{Ca}$  contain a significant admixture of both the prolate and oblate configurations. On the other hand, the  $0_1^+$  collective wave functions of  $^{40}\text{Mg}$  and  $^{42}\text{Si}$  are located inside the prolate and oblate wells, respectively. For spins higher than  $I=0$  the collective wave functions of the ground state band are mostly localized inside the prolate wells for  $^{38,40,42}\text{S}$ . For the nucleus  $^{44}\text{S}$  the  $2_1^+$  collective wave function shows, like its ground state, a significant admixture of the oblate and prolate configurations. A band crossing takes place at the spin value  $I=4$  in  $^{44}\text{S}$  and from there on the

ground state band remains prolate. The ground state bands of  $^{46}\text{Ar}$  and  $^{48}\text{Ca}$  remain oblate deformed up to  $I=6$  and they become prolate for  $I=8$ .

Concerning the first excited states ( $\sigma=2$ ) we notice that the  $0_2^+$  and  $2_2^+$  states in  $^{38,40,42,44}\text{S}$  contain an admixture of the oblate and prolate configurations. For spins higher than  $I=4$  the first excited states ( $\sigma=2$ ) in both  $^{42}\text{S}$  and  $^{44}\text{S}$  are almost located inside the oblate wells. For  $I \geq 4$  the first excited band in  $^{38}\text{S}$  shows a behavior reminiscent of a  $\beta$ -vibrational band: it is located inside the prolate well with a node at a  $q_{20}$  value near the point where the ground state collective wave function attains its maximum value. However, this excited band cannot be considered as a pure  $\beta$ -vibrational band since the corresponding collective wave function is not symmetric around the node. The same pattern is also seen in  $^{40}\text{S}$  but the  $\beta$ -like band in this case appears at  $I=6$ . The excited bands in  $^{40}\text{Mg}$  and  $^{42}\text{Si}$  are located inside the oblate and prolate wells, respectively. The  $0_2^+$  states in  $^{46}\text{Ar}$  and  $^{48}\text{Ca}$  and also the  $2_2^+$  state in  $^{46}\text{Ar}$  contain a significant admixture of the oblate and prolate configurations. For the spin value  $I=8$  the excited bands in  $^{46}\text{Ar}$  and  $^{48}\text{Ca}$  become oblate.

For a more quantitative understanding of the AMPGCM collective wave functions discussed above, the averaged quadrupole moment  $\bar{q}_{20}^{I,\sigma}$  defined as

$$\bar{q}_{20}^{I,\sigma} = \int dq_{20} |g_{\sigma}^I(q_{20})|^2 q_{20}$$


 FIG. 7. Same as Fig. 6 but for the nuclei  $^{40}\text{Mg}$ ,  $^{42}\text{Si}$ ,  $^{46}\text{Ar}$ , and  $^{48}\text{Ca}$ .

is introduced. It provides us with a measure of the quadrupole deformation of the intrinsic state associated with each of the AMPGCM states  $|\Psi_{\sigma}^I\rangle$ . In Table I we give the numerical values (in barns) for all the states considered.

We observe that the  $0_1^+$  ground state in  $^{38}\text{S}$  is nearly spherical with  $\bar{q}_{20}^{0,1} = 0.12$  b ( $\beta_2 = 0.04$ ) and the absolute value of deformation increases in sulfur isotopes up to the value  $|\bar{q}_{20}^{0,1}| = 0.41$  b ( $|\beta_2| = 0.12$ ) in  $^{44}\text{S}$ . The deformation values in  $^{40}\text{Mg}$ ,  $^{42}\text{Si}$ ,  $^{46}\text{Ar}$ , and  $^{48}\text{Ca}$  are  $\bar{q}_{20}^{0,1} = 1.17$  b ( $\beta_2 = 0.35$ ),  $\bar{q}_{20}^{0,1} = -0.93$  b ( $\beta_2 = -0.27$ ),  $\bar{q}_{20}^{0,1} = -0.30$  b ( $\beta_2 = -0.08$ ), and  $\bar{q}_{20}^{0,1} = 0.0$  b, respectively. From these results we conclude that the absolute values of the deformation in the  $N=28$  isotones decrease towards the spherical shell

closure in  $^{48}\text{Ca}$ . This clearly indicates that the  $N=28$  magic number still persists in the very neutron-rich regime near  $^{48}\text{Ca}$ , in good agreement with the shell model predictions (see, for example, Ref. [26]). Another interesting aspect of our results is that the doubly magic spherical ground state of  $^{48}\text{Ca}$  is described in our framework in terms of an intrinsic state, which is a linear combination (with nearly the same weights) of prolate and oblate configurations, which is spherical only on the average. In spite of that, we still consider  $^{48}\text{Ca}$  to be a (highly correlated) closed shell nucleus. The reason is that the collective wave function for the ground state is localized in the interval of quadrupole deformation between  $-1$  and  $1$  b. In this interval, the intrinsic wave functions correspond to configurations in which all the

 TABLE I. The average intrinsic quadrupole moment  $\bar{q}_{20}^{I,\sigma}$  in b for the nuclei  $^{38,40,42,44}\text{S}$  and  $^{40}\text{Mg}$ ,  $^{42}\text{Si}$ ,  $^{46}\text{Ar}$ , and  $^{48}\text{Ca}$ .

Nucleus	$\bar{q}_{20}^{-0,1}$	$\bar{q}_{20}^{-0,2}$	$\bar{q}_{20}^{-2,1}$	$\bar{q}_{20}^{-2,2}$	$\bar{q}_{20}^{-4,1}$	$\bar{q}_{20}^{-4,2}$	$\bar{q}_{20}^{-6,1}$	$\bar{q}_{20}^{-6,2}$	$\bar{q}_{20}^{-8,1}$	$\bar{q}_{20}^{-8,2}$
$^{38}\text{S}$	0.12	0.61	0.52	-0.17	0.74	1.06	1.03	1.37	1.52	1.76
$^{40}\text{S}$	0.33	0.49	0.72	0.00	0.86	0.18	0.93	0.91	0.97	1.40
$^{42}\text{S}$	0.35	0.27	0.73	-0.44	0.86	-0.76	0.92	-1.13	0.95	-1.38
$^{44}\text{S}$	-0.41	0.79	-0.44	0.71	1.10	-0.85	1.23	-1.00	1.27	-1.05
$^{40}\text{Mg}$	1.17	-0.69	1.22	-0.87	1.24	-0.93	1.25	-0.97	1.27	-1.00
$^{42}\text{Si}$	-0.93	0.91	-1.01	1.21	-1.03	1.27	-1.06	1.33	-1.08	1.42
$^{46}\text{Ar}$	-0.30	0.07	-0.72	0.89	-0.84	1.33	-0.92	1.49	1.64	-0.99
$^{48}\text{Ca}$	0.00	0.38	-0.61	0.88	-0.93	1.42	-0.91	1.43	1.79	-1.17

TABLE II. Spectroscopic quadrupole moments in  $e \text{ fm}^2$  for  $I=2, 4, 6, 8$  and  $\sigma=1$  and  $\sigma=2$  for the nuclei  $^{38,40,42,44}\text{S}$  and  $^{40}\text{Mg}$ ,  $^{42}\text{Si}$ ,  $^{46}\text{Ar}$ , and  $^{48}\text{Ca}$ . Each column entry corresponds to the pair  $(I, \sigma)$ .

	(2,1)	(2,2)	(4,1)	(4,2)	(6,1)	(6,2)	(8,1)	(8,2)
$^{38}\text{S}$	-13.63	5.25	-22.49	-32.92	-33.43	-48.35	-54.44	-62.86
$^{40}\text{S}$	-16.76	0.51	-24.02	-9.59	-27.47	-31.35	-29.59	-50.24
$^{42}\text{S}$	-16.01	10.50	-22.72	16.87	-25.31	28.80	-26.71	37.09
$^{44}\text{S}$	9.64	-14.17	-25.80	20.12	-30.87	24.76	-33.09	26.12
$^{40}\text{Mg}$	-20.74	14.59	-26.64	19.53	-31.01	23.27	-33.22	25.00
$^{42}\text{Si}$	19.23	-23.12	24.01	-29.21	27.56	-34.62	30.22	-39.76
$^{46}\text{Ar}$	16.70	-17.81	22.55	-35.42	25.28	-45.13	-53.78	26.90
$^{48}\text{Ca}$	13.84	-19.57	26.05	-42.26	27.50	-47.96	-60.19	36.53

orbitals of the doubly magic configuration with  $Z=20$  and  $N=28$  are fully occupied. Therefore, the ground state wave function does not contain admixtures of  $2p-2h$  excitations that would correspond to occupying orbitals from the subshells above the  $Z=20$ ,  $N=28$  shell closure.

For  $I \geq 2$  the ground-state band in  $^{38}\text{S}$  becomes strongly prolate deformed. This is also the case for  $^{40,42}\text{S}$ . In  $^{44}\text{S}$  both the  $0_1^+$  and the  $2_1^+$  states are oblate with deformations  $\approx -0.4$  b and for higher spin values the ground state band becomes strongly prolate deformed with  $\bar{q}_{20}^{I,1} \approx 1$  b. For increasing spin values the ground state bands in  $^{46}\text{Ar}$  and  $^{48}\text{Ca}$  become strongly oblate deformed up to  $I=6$  and then they become strongly prolate with  $\bar{q}_{20}^{8,1} = 1.64$  b and 1.79 b, respectively.

The situation is very interesting in both  $^{40}\text{Mg}$  and  $^{42}\text{Si}$  as the values of  $\bar{q}_{20}^{I,\sigma}$  (and also the values for the spectroscopic quadrupole moments and  $B(E2, I \rightarrow I-2)$  transition probabilities) suggest the existence of well-defined prolate and oblate bands in both nuclei. The occurrence of an oblate ground state band in  $^{42}\text{Si}$  is of particular relevance as ground state oblate bands are usually an exception and not the rule.

In Table II we show the results for the exact spectroscopic quadrupole moments for each of the wave functions  $|\Psi_\sigma^I\rangle$  (no effective charges have been used) of the nuclei considered and  $\sigma=1$  and  $\sigma=2$ . The spectroscopic moments of the ground bands are all negative (positive) in  $^{40}\text{Mg}$  ( $^{42}\text{Si}$ ), indicating prolate (oblate) intrinsic deformations in the whole spin range  $I=2-8$ . Negative values are also obtained in the considered spin range for the ground bands of  $^{38,40,42}\text{S}$ . The values obtained for the spectroscopic quadrupole moments of the  $2_1^+$  states in  $^{40}\text{S}$  and  $^{42}\text{S}$  are  $-16.76$  and  $-16.01 e \text{ fm}^2$ . They compare well with the shell model results [26] of  $-17.1$  and  $-19.2 e \text{ fm}^2$  for these nuclei. Using the spectroscopic moments  $Q^{\text{spect}}(I, \sigma)$  we can compute the total intrinsic quadrupole moments through the usual expression  $\bar{q}_{20}^{I,\sigma} = -(2I+3/2I)(A/Z)Q^{\text{spect}}(I, \sigma)$  based on the rotational approximation. The intrinsic quadrupole moments obtained in this way are in good agreement with the average values  $\bar{q}_{20}^{I,\sigma}$  of Table II although, as expected, some deviations appear for near spherical states.

Finally, the values obtained for the quadrupole moments  $\bar{q}_{20}^{I,\sigma}$  of the intrinsic states can be used to classify each of the physical states obtained in the AMPGCM approach in terms

of bands. To this end, we have plotted in Figs. 8 and 9 the energies of the AMPGCM states  $E_\sigma^I$  in a diagram of energy versus quadrupole moment. Each energy  $E_\sigma^I$  is placed at a  $q_{20}$  value corresponding to  $\bar{q}_{20}^{I,\sigma}$ . In addition, we have plotted the AMPGES for each angular momentum and nuclei to guide the eye. Although all the features observed in these two figures have already been discussed in detail in the previous paragraphs, the advantage of such a representation is that the band structures of each specific nucleus can be seen at a glance.

To finish this section we will make a few comments on the results obtained for the nucleus  $^{40}\text{Mg}$  with the basis increased by one more shell (i.e.,  $N_{\text{osc}}=11$ ). The excitation energies of the members of the ground state rotational band increase by around 10 keV in going from the  $N_{\text{osc}}=10$  to the  $N_{\text{osc}}=11$  calculation. On the other hand, the excitation energies of the members of the excited rotational band decrease on the average by 50 keV. Concerning the  $B(E2)$  transition probabilities, they do not substantially change when the basis is increased. From these results, we conclude that our calculations are well converged concerning the basis size.

#### IV. COMPARISON WITH EXPERIMENTAL RESULTS

The experimental data available in this region are scarce. Typically, the binding energy is a known quantity and in some cases the excitation energy of the lowest-lying  $2^+$  state as well as the  $B(E2)$  transition probability connecting it to the ground state is also known. In the next sections we will compare our results with the experimental data and in some instances we will make predictions for some relevant quantities like the excitation energies of the lowest-lying  $0^+$  excited states.

##### A. Excitation energies and $B(E2)$ transition probabilities

In this section we compare our results for the excitation energy of some relevant states as well as the  $B(E2)$  transition probabilities among them with the available experimental data. The calculated excitation energies of the  $2_1^+$  states (open circles) along with the experimental data (full circles) taken from Refs. [13,14] are plotted in panel (a) of Fig. 10 as a function of the mass number for the sulfur isotopes. Our calculations reproduce quite well the isotopic trend, but the absolute values come out too high as compared with the

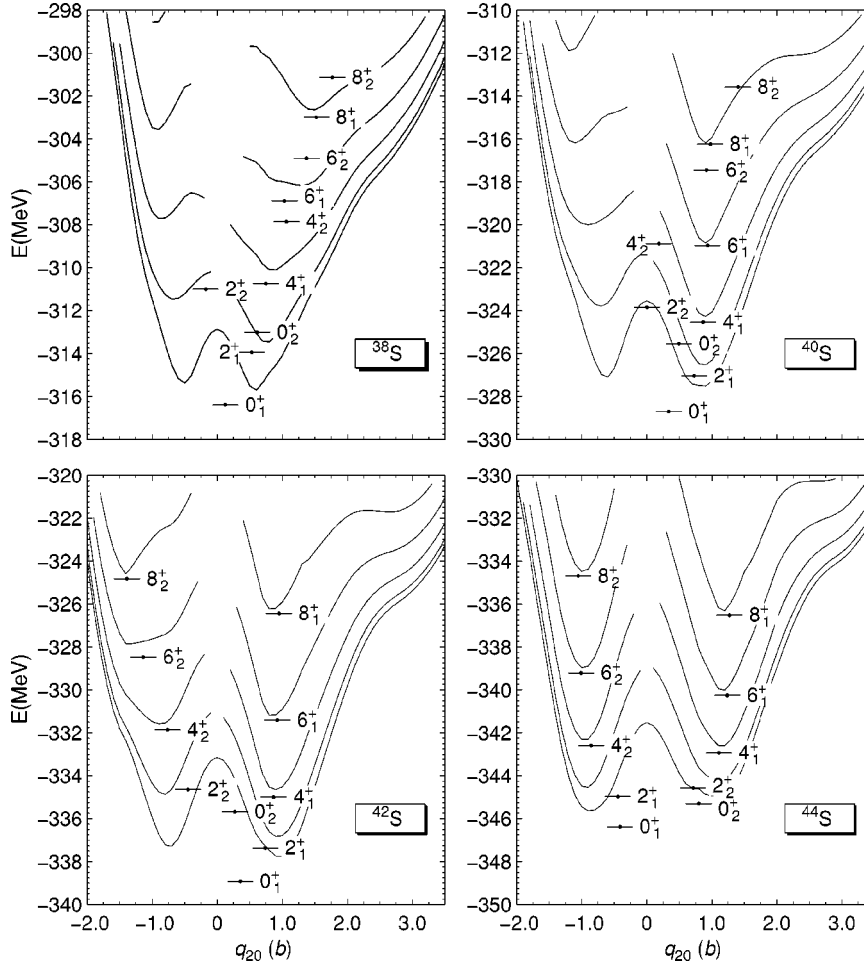


FIG. 8. The AMPGCM energies  $E_{\sigma}^I$  for  $\sigma=1$  and  $2$  and  $I=0, 2, 4, 6,$  and  $8$  are plotted in an energy versus quadrupole moment diagram for the sulfur isotopes. The quadrupole moment of each GCM state is given by the average quadrupole moment  $\bar{q}_{20}^{-I,\sigma}$ . The AMPGES for  $I=0, 2, 4, 6,$  and  $8$  are also plotted to guide the eye.

experiment. In Ref. [30] we also noticed the same behavior in some Mg isotopes (our predictions were systematically too high as compared to the experiment) and attributed it to the lack of time odd  $K \neq 0$  components in our ansatz for the wave function. By using the cranking model we estimated that the effect of incorporating the missing correlations amounts to the use of a quenching factor of 0.7 for the energies of the rotational bands (that is, our results for the excitation energies of the  $2^+$  states should be quenched by such a factor). If the same quenching factor is used for the nuclei considered here we obtain an overall improvement in the comparison with the experimental data. However, one has to be cautious about the use of an overall quenching factor here because it can only be justified for well-deformed prolate rotational bands with strong pairing correlations. Obviously, this is not the situation for the sulfur isotopes considered here and probably a proper treatment of the missing correlations will lead to quenching factors depending on the nucleus under consideration. For this reason we have decided not to incorporate any quenching factor in our results for the excitation energies.

In addition to the  $2_1^+$  excitation energies, we have also plotted in panel (a) of Fig. 10 the calculated excitation energies of the  $0_2^+$  states (open squares). For the  $^{38-42}\text{S}$  isotopes we obtain rather high values for those energies (around 3 MeV) but for  $^{44}\text{S}$  the excitation energy of the  $0_2^+$  (1.07 MeV)

drops below that of the  $2_1^+$  state (1.41 MeV). This is a consequence of the strong shape coexistence obtained for the ground state of this nucleus, and therefore the appearance of such an excited state located at a rather low excitation energy can be considered as a fingerprint of shape coexistence. Such a low-lying  $0_2^+$  excited state has also been obtained in the shell model calculations of Ref. [26] at an excitation energy of 1.51 MeV, which is in reasonable agreement with our result. Besides the theoretical predictions, there is experimental evidence for shape coexistence in the neighboring  $^{43}\text{S}$  isotope that has been obtained in recent intermediate energy Coulomb excitation experiments [15,16] (see Ref. [43] for a shell model calculation).

Concerning the  $B(E2)$  transition probabilities shown in panel (b) of Fig. 10 we notice that they also follow rather nicely the isotopic trend although they show up a little bit too high. The agreement with experiment is rather satisfactory, especially taking into account that no refitting of the force parameters has been carried out, and also taking into account that with the same set of parameters as the ones used here, one can reproduce in a very satisfactory way lots of properties of heavy nuclei. Finally, it has to be mentioned again that our calculations of the  $B(E2)$  transition probabilities do not involve any kind of effective charge.

In Fig. 11 we show the same quantities as in Fig. 10 but for the  $N=28$  isotonic chain. As observed in this figure, we

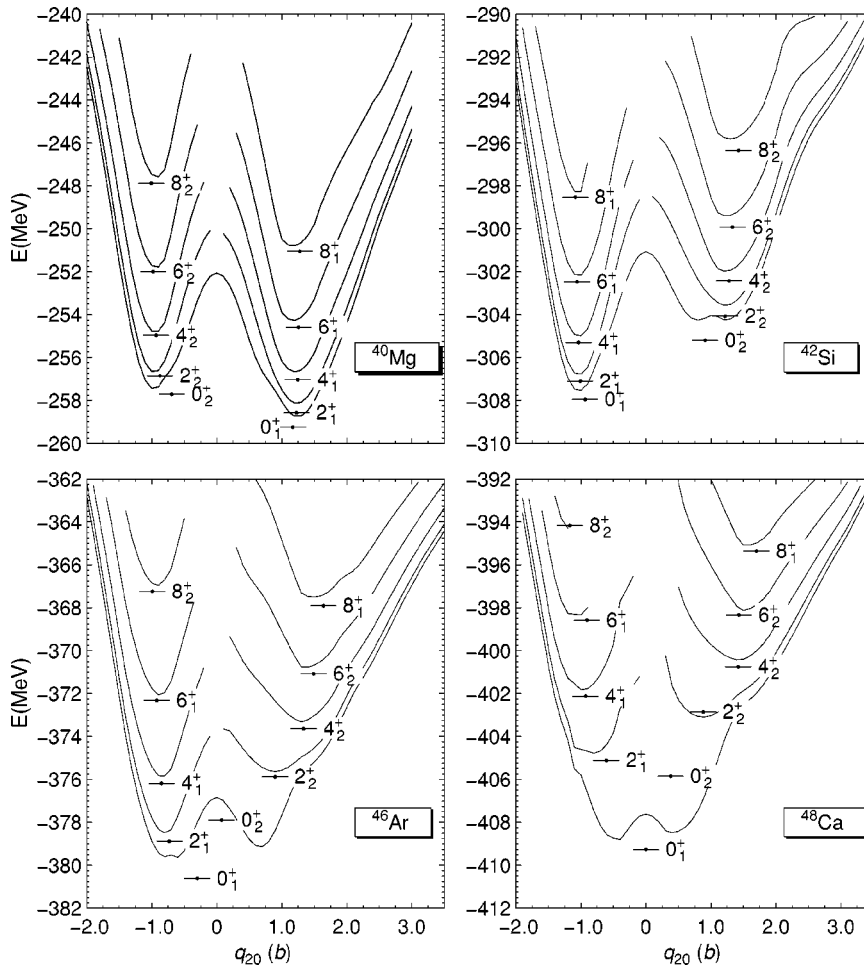


FIG. 9. Same as Fig. 8 but for the  $N=28$  isotones.

reproduce quite well both the  $2_1^+$  excitation energies [panel (a)] of  $^{48}\text{Ca}$ ,  $^{46}\text{Ar}$ , and  $^{44}\text{S}$ , and their  $B(E2)$  transition probabilities [panel (b)]. Concerning the prolate deformed  $^{40}\text{Mg}$  and the oblate deformed  $^{42}\text{Si}$  isotones, where no experimental data are available, our results are comparable with those of the shell model calculations of Refs. [6,26] and the more recent of Ref. [43]. In the later reference, new experimental data obtained for  $^{35}\text{Si}$  have been used to readjust the monopole part of the shell model interaction. Most of the results with the new interaction are similar to the old ones [26] except for the case of  $^{42}\text{Si}$  where the  $2_1^+$  state has an excitation energy that is lower (1.49 MeV with the new interaction versus 2.56 MeV with the old one) and a bigger  $B(E2)$  transition probability to the ground state. The new shell model results are in better agreement with ours and confirm that  $^{42}\text{Si}$  has to be considered as an oblate deformed nucleus. In the  $^{48}\text{Ca}$  nucleus there is also an experimentally observed  $0_2^+$  excited state at an excitation energy of 4.283 MeV. Our prediction for such a state (3.41 MeV) is a little bit lower than experiment, but nevertheless the result is quite satisfactory owing to the parameter-free character of the calculations.

### B. Two neutron separation energies

It is obvious that, as the AMPGCM ground state wave function is more general than the angular momentum pro-

jected wave functions or the HFB ones, the energy of the AMPGCM ground state is going to be lower than that for the other two approaches. The energy gain at spin  $I=0$  with respect to the AMP minimum is 0.68, 1.19, 1.17, and 0.74 MeV for  $^{38}\text{S}$ ,  $^{40}\text{S}$ ,  $^{42}\text{S}$ , and  $^{44}\text{S}$  and 0.52, 0.41, 0.96, and 0.44 MeV for  $^{40}\text{Mg}$ ,  $^{42}\text{Si}$ ,  $^{46}\text{Ar}$ , and  $^{48}\text{Ca}$ , respectively. As the energy gain due to AMPGCM is different for each nucleus, it will affect the predictions for the two neutron and two proton separation energies.

In Table III we show the results obtained for the two neutron  $S_{2n}$  and two proton  $S_{2p}$  separation energies in the nuclei considered for the different approximations used in the present study. In the determination of the values of  $S_{2n}$  and  $S_{2p}$  the Coulomb exchange contribution has been considered at the end of the calculations in a perturbative fashion [33]. First we can observe that the values of  $S_{2n}$  and  $S_{2p}$  do not change significantly with the different theoretical approaches considered with the exception of the  $S_{2p}$  for  $^{48}\text{Ca}$ , which is reduced by almost 2 MeV in going from the HFB to the AMPGCM approach. This reduction brings the theoretical prediction (AMPGCM) for  $^{48}\text{Ca}$  in much closer agreement with the experimental result. Finally, the results obtained with the AMPGCM agree rather well with the available experimental data of Refs. [44,16]. Again, the agreement with the experimental data gives us some confidence on the suitability of both the technique and the inter-

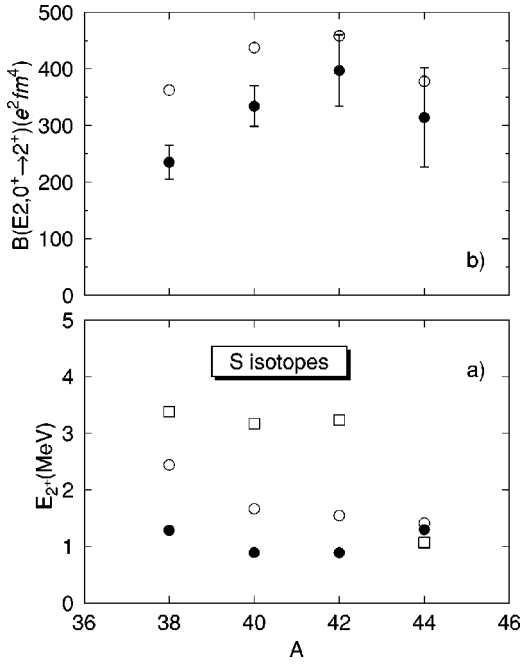


FIG. 10. In panel (a) the excitation energies of the lowest-lying states of the sulfur isotopes are shown. The  $2_1^+$  excitation energies are plotted as circles (full, experimental data; open, theoretical results from our AMPGCM calculations), and the results for the AMPGCM excitation energies of the excited  $0_2^+$  state are plotted as open squares. The  $B(E2, 0_1^+ \rightarrow 2_1^+)$  transition probabilities in units of  $e^2 \text{fm}^4$  are shown in panel (b) for the sulfur isotopes (full circles: experimental data; open ones: AMPGCM results).

action used in this paper for the description of the physics of neutron-rich light nuclei.

## V. CONCLUSIONS

We have studied the properties of the lowest-lying collective states of the neutron-rich nuclei  $^{38-44}\text{S}$  and  $^{40}\text{Mg}$ ,  $^{42}\text{Si}$ ,  $^{46}\text{Ar}$ , and  $^{48}\text{Ca}$  with the angular momentum projected generator coordinate method and the quadrupole moment as collective coordinate. The Gogny force with the D1S set of parameters has been used. The agreement of the theoretical results for excitation energies and  $B(E2)$  transition probabilities with the available experimental data is fairly good, taking into account the parameter-free character of the calculation. In  $^{40}\text{Mg}$  we find a prolate ground state rotational band and an oblate excited rotational band. In  $^{42}\text{Si}$  the situation is reversed and the ground state rotational band is ob-

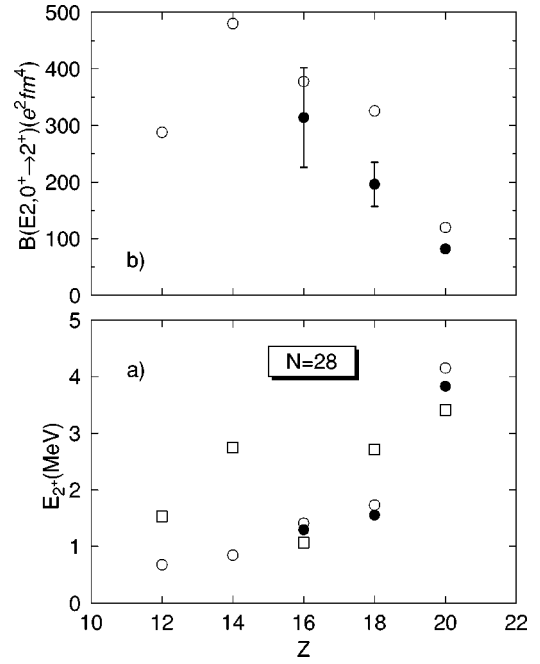


FIG. 11. Same as Fig. 10 but for the  $N=28$  isotones.

late, whereas the excited band is prolate. In  $^{44}\text{S}$  we find strong shape coexistence in the ground state that reflects itself in the appearance of a very-low-lying  $0^+$  excited state. The nucleus  $^{46}\text{Ar}$  can also be considered as a, not so clear, example of shape coexistence whereas  $^{48}\text{Ca}$  is found to be spherical. For the sulfur isotopes we find  $^{38}\text{S}$ ,  $^{40}\text{S}$ , and  $^{42}\text{S}$  to be slightly prolate deformed. A good agreement between the computed and experimentally observed two-neutron and two-proton separation energies is also found.

Another important conclusion is that the mean field description of these nuclei is substantially modified by the effect of restoring the rotational symmetry and also by the correlations induced by the mixing of configurations with different quadrupole moments. Therefore, we find rather inappropriate the use of a mean field description for the nuclei considered here.

## ACKNOWLEDGMENTS

One of us (R.R.-G.) kindly acknowledges the financial support received from the Spanish Instituto de Cooperación Iberoamericana (ICI). This work was supported in part by the DGICYT (Spain) under Project No. PB97/0023.

TABLE III. Two neutron  $S_{2n}$  and two proton  $S_{2p}$  separation energies (in MeV) for the nuclei considered. The experimental values have been taken from Refs. [44,16].

$S_{2n}$	$^{40}\text{S}$	$^{42}\text{S}$	$^{44}\text{S}$	$S_{2p}$	$^{42}\text{Si}$	$^{44}\text{S}$	$^{46}\text{Ar}$	$^{48}\text{Ca}$
HFB	11.79	10.06	7.50	HFB	48.20	38.54	34.55	30.77
AMP	11.80	10.26	7.88	AMP	48.80	38.10	34.00	29.17
AMPGCM	12.31	10.22	7.46	AMPGCM	48.70	38.42	34.23	28.65
Expt.	12.13	10.53	7.61	Expt.	-	-	35.18	29.07

- [1] C. Thibault, R. Klapisch, C. Rigaud, A. M. Poskanzer, R. Prieels, L. Lessard, and W. Reisdorf, *Phys. Rev. C* **12**, 644 (1975).
- [2] D. Guillemaud-Muller *et al.*, *Nucl. Phys.* **A426**, 37 (1984).
- [3] T. Motobayashi *et al.*, *Phys. Lett. B* **346**, 9 (1995).
- [4] A. Poves and J. Retamosa, *Phys. Lett. B* **184**, 311 (1987).
- [5] A. Poves and J. Retamosa, *Nucl. Phys.* **A571**, 221 (1994).
- [6] E. Caurier, F. Nowacki, A. Poves, and J. Retamosa, *Phys. Rev. C* **58**, 2033 (1998).
- [7] X. Campi, H. Flocard, A. K. Kerman, and S. Koonin, *Nucl. Phys.* **A251**, 193 (1975).
- [8] M. Barranco and R. J. Lombard, *Phys. Lett. B* **78**, 542 (1978).
- [9] R. Bengtsson, P. Moller, J. R. Nix, and J. Zhang, *Phys. Scr.* **2**, 402 (1984).
- [10] J. F. Berger *et al.*, *Inst. Phys. Conf. Ser.* **132**, 487 (1993).
- [11] O. Sorlin *et al.*, *Phys. Rev. C* **47**, 2941 (1993).
- [12] M. Lewitowicz *et al.*, *Nucl. Phys.* **A496**, 477 (1989).
- [13] H. Scheit *et al.*, *Phys. Rev. Lett.* **77**, 3967 (1996).
- [14] T. Glasmacher *et al.*, *Phys. Lett. B* **395**, 163 (1997); T. Glasmacher, *Nucl. Phys.* **A630**, 278c (1998).
- [15] R. W. Ibbotson, T. Glasmacher, P. F. Mantica, and H. Scheit, *Phys. Rev. C* **59**, 642 (1999).
- [16] F. Sarazin *et al.*, *Phys. Rev. Lett.* **84**, 5062 (2000).
- [17] T. R. Werner, J. A. Sheikh, W. Nazarewicz, M. R. Strayer, A. S. Umar, and M. Misu, *Phys. Lett. B* **335**, 259 (1994).
- [18] T. R. Werner *et al.*, *Nucl. Phys.* **A597**, 327 (1996).
- [19] M. Beiner *et al.*, *Nucl. Phys.* **A238**, 29 (1975).
- [20] M. M. Sharma, M. A. Nagarajan, and P. Ring, *Phys. Lett. B* **312**, 377 (1993).
- [21] D. Hirata, K. Sumiyoshi, B. V. Carlson, H. Toki, and I. Tanihata, *Nucl. Phys.* **A609**, 131 (1996).
- [22] G. A. Lalazissis, D. Vretenar, P. Ring, M. Stoitsov, and L. M. Robledo, *Phys. Rev. C* **60**, 014310 (1999).
- [23] B. V. Carlson and D. Hirata, *Phys. Rev. C* **62**, 054310 (2000).
- [24] P.-G. Reinhard, D. J. Dean, W. Nazarewicz, J. Dobaczewski, J. A. Maruhn, and M. R. Strayer, *Phys. Rev. C* **60**, 014316 (1999).
- [25] S. Perú, M. Girod, and J. F. Berger, *Eur. Phys. J. A* **9**, 35 (2000).
- [26] J. Retamosa, E. Caurier, F. Nowacki, and A. Poves, *Phys. Rev. C* **55**, 1266 (1997).
- [27] J. Dechargé and D. Gogny, *Phys. Rev. C* **21**, 1568 (1980).
- [28] J. F. Berger, M. Girod, and D. Gogny, *Nucl. Phys.* **A428**, 23c (1984).
- [29] R. Rodríguez Guzmán, J. L. Egido, and L. M. Robledo, *Phys. Lett. B* **474**, 15 (2000).
- [30] R. Rodríguez Guzmán, J. L. Egido, and L. M. Robledo, *Phys. Rev. C* **62**, 054319 (2000).
- [31] R. Rodríguez Guzmán, J. L. Egido, and L. M. Robledo, *nucl-th/0103077*; *Acta Phys. Pol. B* **32**, 2385 (2001).
- [32] M. C. Mermaz and M. Girod, *Phys. Rev. C* **53**, 1819 (1996).
- [33] R. Rodríguez Guzmán, J. L. Egido, and L. M. Robledo, *Phys. Rev. C* **62**, 054308 (2000).
- [34] P.-H. Heenen, P. Bonche, S. Cwiok, W. Nazarewicz, and A. Valor, *RIKEN Rev.* **26**, 31 (2000).
- [35] A. Valor, P.-H. Heenen, and P. Bonche, *Nucl. Phys.* **A671**, 145 (2000).
- [36] L. M. Robledo, *Phys. Rev. C* **50**, 2874 (1994).
- [37] J. L. Egido, L. M. Robledo, and Y. Sun, *Nucl. Phys.* **A560**, 253 (1993).
- [38] R. G. Nazmitdinov, L. M. Robledo, P. Ring, and J. L. Egido, *Nucl. Phys.* **A596**, 53 (1996).
- [39] P. Ring and P. Schuck, *The Nuclear Many Body Problem* (Springer, Berlin, 1980).
- [40] K. Hara and Y. Sun, *Int. J. Mod. Phys. E* **4**, 637 (1995).
- [41] K. Hara, A. Hayashi, and P. Ring, *Nucl. Phys.* **A385**, 14 (1982).
- [42] P. Bonche, J. Dobaczewski, H. Flocard, P.-H. Heenen, and J. Meyer, *Nucl. Phys.* **A510**, 466 (1990).
- [43] S. Nummela *et al.*, *Phys. Rev. C* **63**, 044316 (2000).
- [44] G. Audi and A. H. Wapstra, *Nucl. Phys.* **A595**, 409 (1995).
- [45] The definition used for the intrinsic quadrupole moment is a factor  $\frac{1}{2}$  smaller than the usual definition for this quantity.